Physics Laboratory
Digital Imaging

Group 23

Rasera Benedetta (2141189), Errico Antonio Romano (2157550), Magherini Federico (2152811)

`benedetta.rasera@studenti.unipd.it`
`antonioromano.errico@studenti.unipd.it`
`federico.magherini@studenti.unipd.it`

A.A. 2024/2025
Laboratory dates : 19,20 and 21/11/2024

Università degli Studi di Padova

Dipartimento di Fisica e Astronomia "Galileo Galilei"

Master's Degree in Physics

Contents

1 Introduction

The purpose of this experiment is to obtain an esteem of the mass attenuation coefficients of various materials for a 511 keV photons beam and to reconstruct the shape as well as to determine the material of an unknown sample hidden inside a black box.

2 Experimental setup

A ^{22}Na source is placed inside an iron collimator with an opening diameter of 3 cm to produce a photon beam with defined collinear geometry. The radiation emitted by the source is collected by eight detectors, each consisting of an inorganic scintillator made of $B_4Ge_3O_{12}$ with dimensions of $18 \times 15 \times 25\,mm^3$, coupled to Hamamatsu R4124 photomultipliers. The photomultipliers are powered by a CAEN N4721 power supply unit. Iron collimators are placed in front of all detectors to minimize the occurrence of multiple scattering events.

The experimental setup comprises a gamma detector (D1) positioned on one side of the collimator to detect one of the two 511 keV photons emitted from the annihilation of positronium formed during the β^+ decay of ^{22}Na. A vertical linear array of seven gamma detectors (D2 to D8) is placed on the opposite side of the collimator to detect the corresponding pair photon. Detector D1 acts as the tagging detector for the experiment. The signals from the detector anodes are sent to a variable gain amplifier (PHILIPS 777), which amplifies the signals without altering their shape.

A computer-controlled slide, equipped with a step-by-step engine, positions samples at predefined locations between the radioactive source and the linear array of detectors. The measurements are conducted in coincidence mode using the logical trigger condition:

$$D1 \wedge (D2 \vee D3 \vee D4 \vee D5 \vee D6 \vee D7 \vee D8).$$

3 Scintillators calibration

The energy calibration of the gamma detectors is a critical step in ensuring accurate spectroscopic measurements. The calibration process converts the raw ADC channel outputs from the detectors into corresponding energy values, facilitating the interpretation of experimental data and its comparison with theoretical expectations. The experiment used a ^{22}Na radioactive source, which emits two characteristic gamma rays with energies of 511 keV and 1275 keV during positron annihilation and nuclear de-excitation processes, respectively. To initiate calibration, the output signals from the detectors were amplified using the Philips 777 fast amplifier and observed on an oscilloscope. The amplified signals were then connected to a Constant Fraction Discriminator (CFD) to suppress electronic noise and isolate valid events. The CFD threshold was carefully adjusted to balance the exclusion of noise with the retention of meaningful data.

Tab. 1 shows the general characteristics of the signals corresponding to the detection of a photon by the detectors. The order of magnitude of these values was measured using the oscilloscope.

Detector	Polarity (ns)	Rise Time (ns)	Amplitude (mV)
$\forall D$	negative	$1 - 10$	10^3

Table 1. Signal Characteristics

Figure 1. Example of a wave signal.

Spectra for each detector were acquired using a digitizer, with trigger signals provided by coincidence logic involving the tagging detector (D1). The calibration data consisted of two distinct peaks corresponding to the 511 keV and 1275 keV gamma rays, visible in the energy spectrum.

For each detector, the energy spectrum was fitted with Gaussian functions to determine the centroids of the 511 keV and 1275 keV peaks. These centroids, measured in ADC channels, were subsequently used as reference points for calibration. It is worth noting that the peaks in the spectra often deviate from a pure Gaussian shape because of the presence of background events, which contribute a nearly linear component to the signal. Despite this, a Gaussian fit was used for simplicity and

consistency, as this approach is sufficient for the level of accuracy required in this analysis. A linear relationship was assumed between the ADC channel C and the photon energy E (keV):

$$E = a \cdot C + b$$

where a (keV/channel) and b (keV) are calibration constants determined through a least-squares fit of the peak centroids. The calibration results are summarised in the following tables. Tab. 2 reports the fitted parameters for the Gaussian peaks, including amplitude, for each peak of the ^{22}Na spectrum.

Detector	Peak Energy [keV]	Amplitude	μ [ADC]	σ [ADC]	χ^2
D1	511	$(338.1 \pm 1.9) \cdot 10^3$	616.0 ± 0.5	110.8 ± 0.8	357
	1275	$(438 \pm 3) \cdot 10^2$	1624.6 ± 1.3	169.0 ± 1.5	662
D2	511	$(2822 \pm 5) \cdot 10^3$	773.9 ± 0.2	118.2 ± 0.3	1400
	1275	$(511 \pm 2) \cdot 10^3$	1983.4 ± 0.7	217 ± 1	665
D3	511	$(389 \pm 1) \cdot 10^4$	235.3 ± 0.1	39.71 ± 0.16	3334
	1275	$(759 \pm 4) \cdot 10^3$	595.5 ± 0.3	75.3 ± 0.5	528
D4	511	$(367 \pm 2) \cdot 10^4$	446.8 ± 0.4	72.3 ± 0.5	18323
	1275	$(784 \pm 4) \cdot 10^3$	1156.2 ± 0.6	171.2 ± 1.0	545
D5	511	$(362.1 \pm 1.2) \cdot 10^4$	219.3 ± 0.2	48.5 ± 0.2	3069
	1275	$(664 \pm 4) \cdot 10^3$	568.7 ± 0.4	90.6 ± 0.6	467
D6	511	$(4103 \pm 7) \cdot 10^3$	468.4 ± 0.1	84.9 ± 0.2	926
	1275	$(705 \pm 2) \cdot 10^3$	1249.2 ± 0.4	142.1 ± 0.6	485
D7	511	$(266 \pm 8) \cdot 10^3$	166.1 ± 0.5	50 ± 2	74
	1275	$(80 \pm 2) \cdot 10^3$	414 ± 2	74 ± 2	165
D8	511	$(60 \pm 1) \cdot 10^3$	132.1 ± 0.8	42.7 ± 0.8	100
	1275	$(167 \pm 4) \cdot 10^2$	338 ± 2	59 ± 2	210

Table 2. Gaussian Fit Parameters for ^{22}Na Peaks

Finally a linear fit was performed between the two energy points of each detector, obtaining the results shown in Tab. 3 and in Fig. 2. It is not useful to highlight the value of the χ^2 since the fit is done between two points only.

Detector	a [keV/ADC]	b [keV]
D1	0.757 ± 0.002	44 ± 1
D2	0.6316 ± 0.004	22.2 ± 0.3
D3	2.1213 ± 0.0003	11.8 ± 0.1
D4	1.077 ± 0.001	29.8 ± 0.4
D5	2.1866 ± 0.0004	31.4 ± 0.1
D6	0.9785 ± 0.0002	52.7 ± 0.1
D7	3.08 ± 0.02	-1 ± 3
D8	3.71 ± 0.01	21 ± 2

Table 3. Linear fit parameters
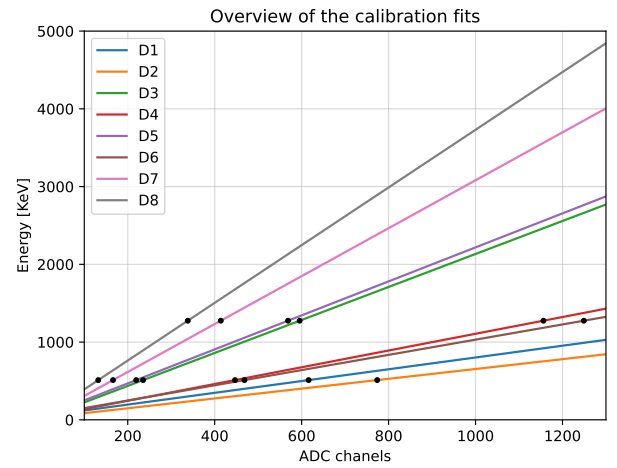
Figure 2. Linear fits of the 8 detectors.

The uncalibrated and calibrated spectra are shown in Fig. 3 below. By comparing the number of counts registered by each detector, therefore the height of each gaussian peak, an evident difference emerges. Such difference is essentially due different trigger settings, which were manually adjusted for each detector to achieve good resolution and high statistics.
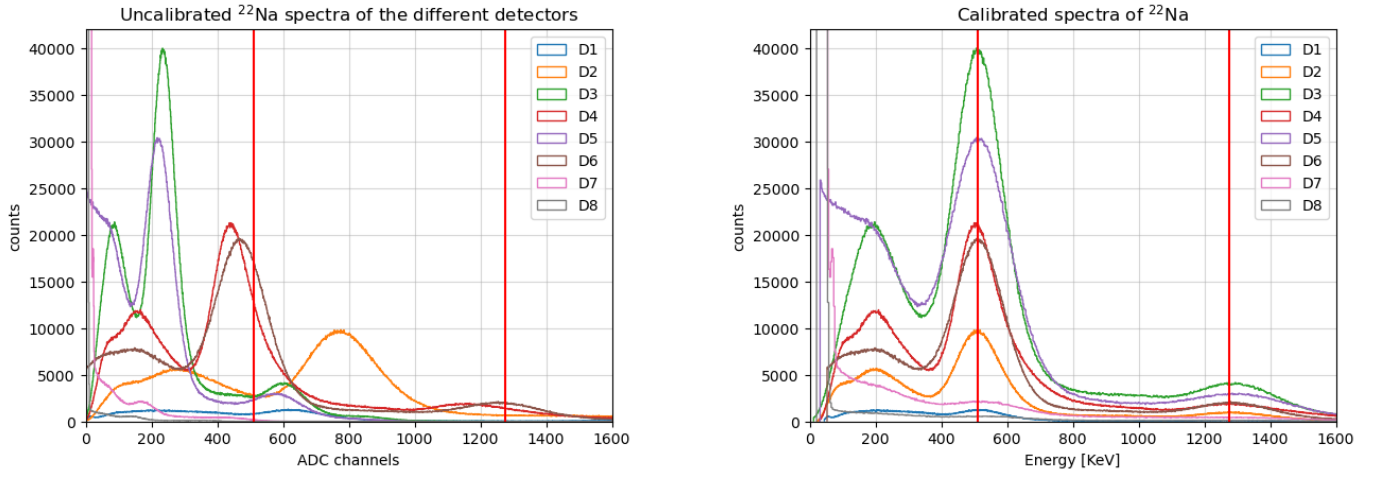
Figure 3. Left: the early uncalibrated detectors spectra. Right: the calibrated spectra obtained as explained above. The red vertical red lines mark the $E_\gamma = 511$ keV and $E_\gamma = 1275$ keV energy values of the gamma photons emitted by the ^{22}Na source.

However, systematic errors in calibration could nevertheless arise from factors such as misalignment of the source and detectors, improper CFD threshold settings, or electronic noise. The calibrated detectors are now prepared for subsequent measurements.

4 Search for coincidences

To verify the capability of the setup to combine signals from detector D1 and any of the other seven detectors, a series of checks were carried out. The inverted output of the Fast Discriminator was connected to channel 1 of the oscilloscope, while the Constant Fraction Timing Discriminator (CFTD) signal of D5 was connected to channel 2. Observing the oscilloscope, it was confirmed that when D5 received a signal, the inverted signal of D1 was null.

The procedure was then repeated by replacing the CFTD output of D5 with the CF8000 OR signal. The CF8000 OR output generates a signal when at least one valid event occurs in one of the eight channels connected to the detector array. This step aimed to confirm that the inverted signal of D1 can serve as the Inhibit input for CF8000. This implies that the OR output of CF8000 is in coincidence with D1, as the CF8000 outputs are enabled only when the signal at the Inhibit input is null. With these verifications completed, the electronics were conFigured for data acquisition. The OR output, filtered by the Inhibit, was split using a T-junction and connected to the TRG IN inputs of the two digitizers.

As the final and necessary step, the ^{22}Na source was moved inside the collimator once again, close to detector D1 and aligned with D5, the central of the other vertically disposed detectors. A test acquisition was performed lasting approximately 10 minutes to ensure proper operation of the electronics and the setup.

4.1 Home Acquisition

Having set the apparatus to look for coincident signals, we performed a data acquisition of 30 minutes without any sample covering the detectors. This configuration is referred to as the home acquisition, corresponding to the cart being at its home position.[1] The counts obtained in this measurement represent I_0 in the attenuation formula, which will be discussed in the following Sec.s. The resulting spectra are shown below, in Fig. 4: the left panel includes all detectors, while the right panel excludes D1. The red vertical line marks the energy $E_\gamma = 511$ keV, corresponding to gamma photons emitted by the ^{22}Na source during positron-electron annihilation.

---

[1]All samples are mounted on a motorised slide controlled by a web based GUI. In order to analyze a specific sample, the slide has to be moved by a precise number of steps in order to cover the vertically aligned detectors. As a result, since the first measurement is performed without any sample in between, namely with the cart at the home position, it will be called *home acquisition*.
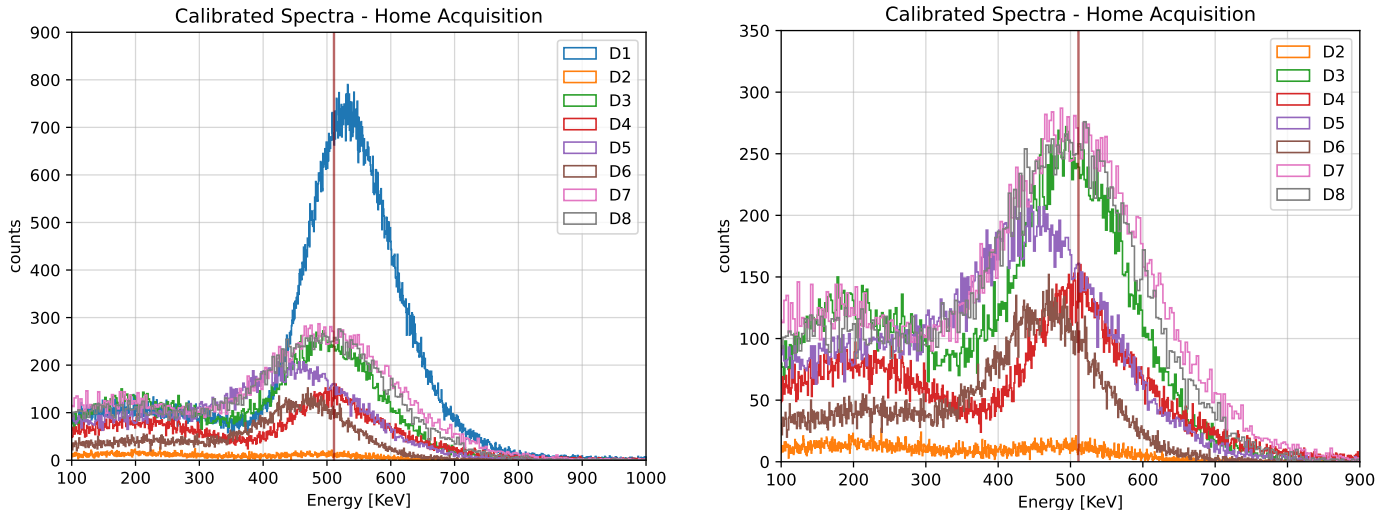
Figure 4. Home acquisition spectra: on the left, we represent the home acquisition spectra for all the detectors; on the right, we represent the home acquisition spectra omitting the D1 detector. The vertical red line marks the $E_\gamma = 511\,\text{keV}$ energy value of the gamma photon emitted by the ^{22}Na source.

The number of counts recorded during this acquisition is noticeably lower than in the energy calibration measurements (see Fig. 3), despite the longer acquisition time. This decrease in counts confirms that the electronics were conFigured correctly for coincidence detection, as uncorrelated signals were strongly suppressed. It is also worth noting that the trigger system starts recording when a signal is detected by one of the vertical detectors (D2 to D8). If no signal is detected in a channel, the digitizer registers an event in channel 0, which is why the spectra in Fig. 4 are truncated at lower energies.

Furthermore, placement of the ^{22}Na source in the collimator (rather than in front of every detector) plays a role in this reduction. In the current setup, the source was positioned closer to D1 and farther from the vertical detectors (D2 to D8). This geometry decreases the probability of coincident photons reaching the vertical detectors, thereby further reducing the counts across all channels.

The relative differences in counts among the vertical detectors (D2 to D8) are another significant observation. As seen in Fig. 2, these variations are primarily due to differences in the manually adjusted trigger thresholds for each detector. However, when comparing the calibration data with the home acquisition spectra in Fig. 4, some additional insights emerge. Detectors D7 and D8, despite having higher threshold values, recorded the highest counts during home acquisition. In contrast, D2, which has a lower threshold, registered fewer counts than the other detectors. This apparent inconsistency can be explained by the geometry of the setup and the role of Compton scattering.

Gamma photons emitted by the ^{22}Na source during positron-electron annihilation are emitted back-to-back. If one photon enters the D1 detection cone, it triggers the coincidence system. The other photon, emitted in the opposite direction, travels towards the vertical detectors. The misalignment between the source, D1, and the vertical array would result in reduced counts for some detectors. The data suggest that D1 and the source are better aligned with D7, as this detector recorded the highest counts while presenting a high threshold. This interpretation is further supported by our sample analysis (see Sec. 5), where detectors D6, D7, and D8 yielded results most consistent with theoretical expectations, while detector D2 exhibited low photon counts and poor compatibility. The influence of Compton scattering, although present, is minimal, due to the relatively short air path and the high energy of the photons.

Another phenomenon observed in the home acquisition spectra is an energy shift compared to the calibration spectra (see Fig. 3). Specifically, the D1 detector exhibits a slight energy increase, while the vertical detectors (D2 to D8) show an overall decrease. This behavior can be attributed to several factors.

- First, the position of the ^{22}Na source in the collimator may have contributed to the shift. Being closer to D1, photons are less likely to scatter in the air, resulting in a higher detected energy. In contrast, the increased distance from the vertical detectors raises the likelihood of Compton scattering with ambient electrons, causing a reduction in the detected energy. However, this contribution is minor, as the mean free path for 511 keV photons in the air is several meters.

- Secondly, the energy calibration performed in the first session may no longer be fully accurate due to changes in the electronic acquisition system or the altered geometry of the setup. Such factors could introduce systematic shifts in the measured energies.

4

Despite these observations, neither the energy shifts nor the count variability affect the subsequent analysis of the samples. The calculation of the attenuation coefficient μ is solely based on the relative fraction I/I_0, making these phenomena irrelevant to the determination of the final results. What may have substantially influenced our analysis is the position of the samples with respect to the collimator and the vertically aligned detectors D2 to D8. As depicted in Fig.5, we placed both the holders and the black box (see Sec. 5 and Sec. 6) closer to the source rather than the detectors. Such choice turned out be crucial in the sample analysis as it lead to unexpected results. Such aspects will be discussed thoroughly in the following sections.

5   Attenuation coefficient of different samples

The attenuation coefficient of various materials was determined using the exponential law of attenuation, as expressed in Eq. 1

$$I = I_0 \, e^{-\mu x} = I_0 \, e^{-\mu_{\text{mass}} \, \rho \, x} \quad \xrightarrow{\text{which leads to}} \quad \mu = -\frac{1}{x} \, \ln\left(\frac{I}{I_0}\right) \tag{1}$$

where μ is the attenuation coefficient, ρ is the material density, and $\mu_{\text{mass}} = \mu/\rho$ is the mass attenuation coefficient. The intensity I is defined as:

$$I = \frac{N}{A \cdot \text{BR}(\gamma) \cdot \epsilon_g \cdot \epsilon_i \cdot t} \tag{2}$$

where N is the total number of counts, A is the activity of the source, $\text{BR}(\gamma)$ is the branching ratio of the 511 keV photons, ϵ_g and ϵ_i are the geometric and intrinsic efficiencies of the detectors, respectively, and t is the acquisition time. The associated uncertainty of the attenuation coefficient μ is given by:

$$\sigma_\mu = \frac{1}{\rho \, x} \sqrt{\left[\ln\left(\frac{N}{N_0}\right)\right]^2 \frac{\sigma_x^2}{x^2} + \frac{\sigma_N^2}{N^2} + \frac{\sigma_{N_0}^2}{N_0^2}} \tag{3}$$

where N_0 is the total number of counts in the home position without the sample. The intensity I is derived from the integral of the fitted Gaussian curve around the 511 keV peak within 2σ.

To compute the effective photon path through the sample, which we will call generically x, we use the relation $x = x_0/\cos\theta$, where x_0 is the horizontal thickness of the sample and θ is the angle between the photon trajectory and the normal to the sample. The effective thickness x_i for each detector is calculated by averaging over all possible paths using the mean value theorem for integrals, as shown in Eq. 4:

$$x_i = \frac{1}{\theta_{i,max} - \theta_{i,min}} \int_{\theta_{i,min}}^{\theta_{i,max}} \frac{x_0}{\cos\theta} \, d\theta = \frac{x_0}{2(\theta_{i,max} - \theta_{i,min})} \left[\ln\left(\frac{1 + \sin\theta_{max,i}}{1 - \sin\theta_{max,i}}\right) - \ln\left(\frac{1 + \sin\theta_{min,i}}{1 - \sin\theta_{min,i}}\right)\right] \tag{4}$$

where the angular limits $\theta_i^{\max}$ and $\theta_i^{\min}$ are given by

$$\begin{cases} \theta_{i,max} &= \arctan\left(\frac{k_i + h}{L}\right) \\ \theta_{i,min} &= \arctan\left(\frac{k_i}{L}\right) \end{cases} \tag{5}$$

with k_i being the lateral position of the i-th detector which depends both on h and d and $L = 250$ mm being the horizontal distance from the source.

The detector layout is illustrated in Fig. 5 below, where the source is aligned with detector D7 as discussed in Sec. 4.1.
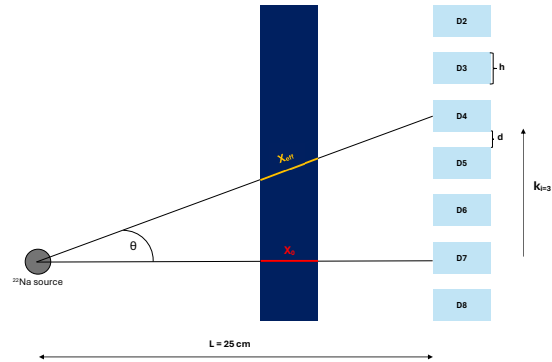
Figure 5. Schematic representation of the detector geometry: $h = 15$ mm represents the height of each detector, and $d = 5$ mm indicates the spacing between adjacent detectors.

For each material, the following steps were carried out in the analysis:

- The attenuation coefficient μ was calculated for each detector. This value was then divided by the material density ρ to obtain the mass attenuation coefficient $\mu_{\text{mass},\,i} = \mu_i / \rho_i$ for each detector.

- The compatibilities between the $\mu_{\text{mass},\,i}$ values from different detectors were evaluated to ensure consistent results across the array, using Eq. 6:

$$r_{i,j} = \frac{|\mu_i - \mu_j|}{\sqrt{\sigma_i^2 + \sigma_j^2}} \tag{6}$$

- The compatibility of the computed values $\mu_{\text{mass},\,i}$ with the reference data of the National Institute of Standards and Technology (NIST, https://www.nist.gov/) was assessed, remembering that the true value $\overline{\mu}$ is considered without any error.

- The final estimate of the mass attenuation coefficient, $\langle \mu_{\text{mass}} \rangle$, was calculated as the weighted average of the individual $\mu_{\text{mass},\,i}$ values, using the inverse of the squared uncertainties as weights. The weighted average and its uncertainty were calculated using:

$$\langle \mu_{\text{mass}} \rangle = \frac{\sum_i \dfrac{\mu_{\text{mass},\,i}}{\sigma_{\mu_{\text{mass},\,i}}^2}}{\sum_i \dfrac{1}{\sigma_{\mu_{\text{mass},\,i}}^2}} \qquad \text{where} \qquad \sigma_{\langle \mu_{\text{mass}} \rangle} = \sqrt{\frac{1}{\sum_i \dfrac{1}{\sigma_{\mu_{\text{mass},\,i}}^2}}} \tag{7}$$

The weighted averaging method reduces overall uncertainty but often worsens compatibility indices due to narrower confidence intervals. For consistency, data from detectors D3 to D8 were included in the calculation, with D7 typically providing the most reliable measurements. This broader approach was necessary to address inconsistencies among the mass attenuation coefficients from different detectors. Although the inclusion of less reliable detectors may cause the weighted average to deviate further from the expected reference value, it remains a statistically robust method that ensures a comprehensive estimate of the mass attenuation coefficient.

Technical issues during the experiment. A preliminary analysis revealed anomalies in the data for the iron and graphite samples, unlike the other materials. This was traced to an error in the initial mounting, where the samples were positioned closer to the source instead of near the detectors. Although this misalignment probably had minimal impact, as the detectors were fully covered, we nonetheless updated the setup geometry.

To resolve the issue, a new 15-minute data acquisition was performed the next day with the samples properly positioned closer to the detectors. Most importantly, the initial one-hour acquisition for these samples was likely affected by interference from a nearby Compton Scattering experiment, which introduced artifacts and unphysical results.

Consequently, the analysis for the iron and graphite samples is based exclusively on the corrected 15-minute acquisition. In contrast, the results for aluminum, polyethylene, and lead rely on their original 30-minute acquisitions, as their setups were correctly aligned. The flawed initial one-hour acquisition data for the iron and graphite samples are summarised and discussed in Appendix 8 for completeness.

5.1 Lead

The lead sample used in this experiment had a measured thickness of $x_0 = (4.8 \pm 0.1)\,\text{mm}$ and a known density of $\varrho_{\text{Pb}} = 0.01135\,\text{g/mm}^3$. The expected value of the mass attenuation coefficient for lead is $\overline{\mu}_{\text{Pb}} = 14.14\,\text{mm}^2/\text{g}$. Using these parameters, the mass attenuation coefficients $\mu_{\text{mass},\,i}$ were calculated for each detector (D2 through D8), along with their compatibility with the theoretical value. The results of this analysis are summarised in Tab. 4; the calibrated spectra for the lead sample are displayed in Fig. 6.

As observed in the analysis of the home acquisition spectra, the results for the lead sample highlight an anomaly in the performance of detector D2. The calculated mass attenuation coefficient for D2 not only shows significant incompatibility with the expected value (see Tab. 4) but also deviates markedly from the results obtained for the other detectors (see Tab. 5). This discrepancy is clearly reflected in the spectra presented in Fig. 6, where detector D2 exhibits a substantially lower count rate compared to the other detectors. In contrast, the mass attenuation coefficient obtained with detector D7 demonstrates excellent agreement with the expected value and with the $\mu_{\text{mass},\,i}$ values of adjacent detectors.

Detector	$\mu_{\mathrm{mass}} \; [\mathrm{mm}^2/\mathrm{g}]$	r
D2	10.5 ± 0.5	11.7
D3	14.1 ± 0.4	5.7
D4	14.3 ± 0.4	4.9
D5	14.5 ± 0.4	4.5
D6	15.2 ± 0.4	2.3
D7	15.7 ± 0.4	1.2
D8	14.9 ± 0.4	2.9

Table 4. Calculated values of $\mu_{\mathrm{mass}, \, i}$ for each detector, along with their compatibility indices r. The best agreement with the expected value is observed for D7, consistent with its alignment with both the source and D1.
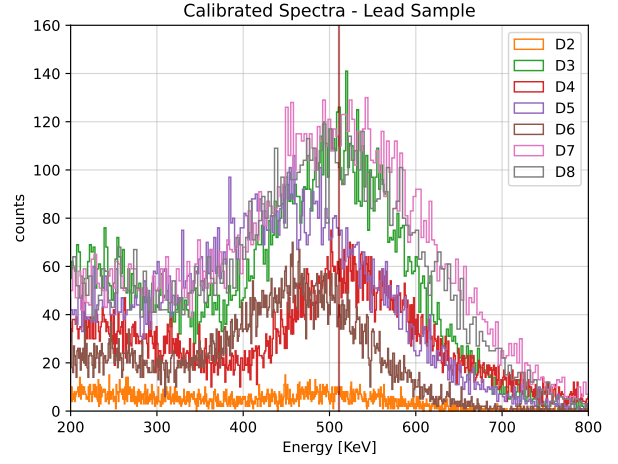
Figure 6. Calibrated spectra for the lead sample, excluding the D1 spectrum. Detector D2 displays the lowest count rate, further supporting the hypothesis of alignment issues, whereas D7 shows minimal energy shift, indicating optimal alignment with the source and D1.

Furthermore, a detailed examination of the spectra in Fig. 6 reveals a noticeable energy shift to the left (lower energies) across all detectors (D2 to D8). Although there are some exceptions, such as D3 and D4, the energy shift appears to become more pronounced with increasing distance from D7. This trend is correlated with longer effective penetration lengths, x_{eff}. The observed energy reduction is consistent with the effects of Compton scattering, as discussed in Sec. 4.1, where energy loss increases with larger photon deviation angles. It is important to note that, in contrast to the home acquisition spectra, Compton scattering plays a more significant role in this case. The photons now traverse a material with a higher atomic number Z and higher density, conditions that enhance the probability and impact of scattering interactions, leading to greater energy loss.

Pb	D2	D3	D4	D5	D6	D7	D8
D2		6.03	6.32	6.53	7.61	8.22	7.03
D3	6.03		0.44	0.71	2.12	2.88	1.52
D4	6.32	0.44		0.27	1.67	2.43	1.09
D5	6.53	0.71	0.27		1.40	2.16	0.83
D6	7.61	2.12	1.67	1.40		0.74	0.54
D7	8.22	2.88	2.43	2.16	0.74		1.27
D8	7.03	1.52	1.09	0.83	0.54	1.27	

Table 5. Compatibilities of the attenuation coefficients for the lead sample between different detectors. Compatibility values below or equal to 3 are shaded in `blue`; values above 3 are shaded in `red`, with a proportional saturation.

These findings suggest that D7 is optimally aligned with the source and D1, while D2 is the farthest from the source in the experimental setup. This conclusion is further supported by the cross-compatibility analysis of the mass attenuation coefficients, as shown in Tab. 5. The value of $\mu_{\mathrm{mass}, \, i}$ for D2 is highly inconsistent with the values of the other detectors, reinforcing the misalignment hypothesis.

Consequently, the $\mu_{\mathrm{mass}, \, i}$ value for D2 was excluded from the calculation of the weighted average mass attenuation coefficient. In conclusion, the mass attenuation coefficient of lead is $\langle \mu_{\mathrm{mass}}^{\mathrm{Pb}} \rangle = (14.7 \pm 0.2) \; \mathrm{mm}^2/\mathrm{g}$ with a compatibility respect to the true value of $\mathrm{r_{Pb}} = 9.02$.
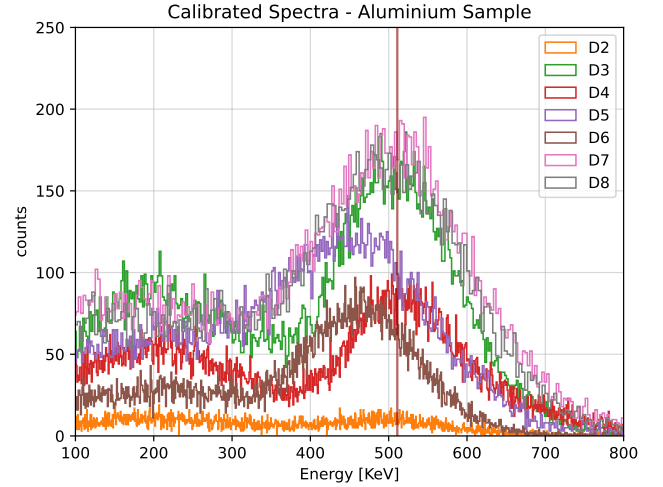
5.2 Aluminium

The aluminium sample had a measured thickness of $x_0 = (20.0 \pm 0.1)$ mm and a known density of $\varrho_{\text{Al}} = 0.0027\,\text{g/mm}^3$. The expected value of the mass attenuation coefficient for aluminium is $\overline{\mu}_{\text{Al}} = 8.445\,\text{mm}^2/\text{g}$. Using these parameters, the mass attenuation coefficients $\mu_{\text{mass},\,i}$ were calculated for each detector (D2 through D8), along with their compatibility with the theoretical value. The results are summarised in Tab. 6, while the calibrated spectra are displayed in Fig. 7.

Detector	μ_{mass} [mm^2/g]	r
D2	2.2 ± 0.4	16.98
D3	7.2 ± 0.2	6.99
D4	7.6 ± 0.2	4.54
D5	7.8 ± 0.2	3.45
D6	8.2 ± 0.2	1.38
D7	8.6 ± 0.2	0.59
D8	7.5 ± 0.2	4.33

Table 6. Calculated values of $\mu_{\text{mass},\,i}$ for each detector and their corresponding compatibility indices r. The compatibility coefficients indicate strong agreement for detectors D6, D7, and D8, which are better aligned with the source. Conversely, detector D2 exhibits significant incompatibility with the true value.

Figure 7. Calibrated spectra for the aluminium sample, excluding the D1 spectrum. Once again, the D2 detector displays the lowest count rate.

As observed in the previous case, the aluminum sample exhibits a similar trend. The mass attenuation coefficient calculated for detector D2 is incompatible with the expected value (see Tab. 6) and deviates significantly from the results obtained with the other detectors (see Tab. 7). In contrast, the mass attenuation coefficient measured with detector D7 shows excellent agreement with the expected value and aligns closely with the $\mu_{\text{mass},\,i}$ values of adjacent detectors.

Al	D2	D3	D4	D5	D6	D7	D8
D2		12.06	13.00	13.55	14.30	15.25	12.35
D3	12.06		1.60	2.43	3.76	5.20	1.17
D4	13.00	1.60		0.80	2.16	3.58	0.31
D5	13.55	2.43	0.80		1.38	2.81	1.05
D6	14.30	3.76	2.16	1.38		1.39	2.30
D7	15.25	5.20	3.58	2.81	1.39		3.62
D8	12.35	1.17	0.31	1.05	2.30	3.62	

Table 7. Compatibilities of the attenuation coefficients for the aluminium sample between different detectors. Compatibility values below 3 are shaded in `blue`; values above 3 are shaded in `red`, with proportional saturation.

The spectra shown in Fig. 7 reveal a consistent energy shift toward lower energies across all detectors, replicating the trend observed in the lead sample analysis (Sec. 5.1). The key difference lies in the increased count rates in the aluminum spectra, which is expected due to aluminum lower mass attenuation coefficient. This result reflects the reduced probability of photon interaction in aluminum compared to lead, resulting in less attenuation.

As with the lead sample, the results indicate that detector D7 is optimally aligned with the source and D1, while detector D2 is the farthest from the source in the experimental setup. Consequently, the $\mu_{\text{mass},\,i}$ value for D2 was excluded from the weighted average calculation. Using the data from the remaining detectors, the final estimate for the mass attenuation coefficient of aluminum is $\langle \mu_{\text{mass}}^{\text{Al}} \rangle = (7.79 \pm 0.08)\,\text{mm}^2/\text{g}$ with a compatibility index with the true value of $r_{\text{Al}} = 8.28$.

5.3 Polyethylene

The polyethylene sample, also known as **PE** or $(C_2H_4)_n$, had a measured thickness of $x_0 = (21.0 \pm 0.1)$ mm, and a known density of $\varrho_{\text{PE}} = 0.00093\,\text{g/mm}^3$. The expected mass attenuation coefficient for polyethylene is $\overline{\mu}_{\text{mass}}^{\text{PE}} = 9.947$ mm^2 / g. Using these parameters, the mass attenuation coefficients $\mu_{\text{mass},\,i}$ were calculated for each detector (D2 through D8), together with their compatibility with the theoretical value. The results, summarised in Tab. 8, reveal a behavior that is radical different from previous samples, as all detectors exhibit poor compatibility with the expected mass attenuation coefficient for polyethylene.

The cross-compatibility analysis in Tab. 9 highlights an overall lack of agreement between the mass attenuation coefficients obtained from different detectors. This inconsistency suggests potential misalignment of the sample (not fully covering all detectors) or defects within the material itself. However, the good compatibility observed among detectors D6, D7, and D8 raises further questions, not only about the experimental configuration but also about the material's composition.

To investigate further, the measured mass attenuation coefficients were compared with the expected values for other thermoplastic polymers similar to polyethylene (**PE**). The best candidates were identified as **PET** $(C_{10}H_8O_4)_n$, with a known density of $\varrho_{\mathrm{PET}} = 1.38 \cdot 10^{-3}\,\mathrm{g/mm^3}$ and expected mass attenuation coefficient $\overline{\mu}_{\mathrm{mass}}^{\mathrm{PET}} = 9.079\ \mathrm{mm^2/g}$, and **ABS** $(C_8H_8 \cdot C_4H_6 \cdot C_3H_3N)_n$ with a known density of $\varrho_{\mathrm{ABS}} = 1.07 \cdot 10^{-3}\,\mathrm{g/mm^3}$ and expected value mass attenuation coefficient of $\overline{\mu}_{\mathrm{mass}}^{\mathrm{ABS}} = 11.87\ \mathrm{mm^2/g}$.

Among these materials, ABS appears to fit the data best, as indicated in Tab. 8. However, even detectors D6, D7, and D8 (the most reliable due to their alignment with the source and D1) show poor compatibility with ABS. Assuming that the material is indeed ABS, the measured mass attenuation coefficients suggest an effective thickness of approximately $\tilde{x}_0 \approx 28.0\,\mathrm{mm}$. This discrepancy prevents a confident identification of the composition of the sample and points to a combination of potential issues, including misalignment, material defects, and experimental uncertainties.

The discrepancy may also be attributed to the placement of the sample holder, as discussed in Sec. (5). Because this positioning did not significantly impact the results for the lead and aluminum samples, it is reasonable to expect a similar outcome for the polyethylene sample. However, positioning the sample farther from the detectors may have made the alignment process more challenging, potentially resulting in incomplete detector coverage. Unfortunately, due to time constraints, we were unable to perform a new acquisition with the sample holder repositioned closer to the detectors, leaving this issue unresolved.

Detector	$\mu_{\mathrm{mass}}^{\mathrm{PE}}\ [\mathrm{mm^2/g}]$	r (PE)	$\mu_{\mathrm{mass}}^{\mathrm{PET}}\ [\mathrm{mm^2/g}]$	r (PET)	$\mu_{\mathrm{mass}}^{\mathrm{ABS}}\ [\mathrm{mm^2/g}]$	r (ABS)
D2	0.7 ± 1.0	9.39	0.4 ± 0.7	12.96	0.6 ± 0.9	13.15
D3	16.0 ± 0.5	12.25	10.8 ± 0.3	5.10	13.9 ± 0.4	4.73
D4	14.3 ± 0.5	8.72	9.6 ± 0.3	1.67	12.4 ± 0.4	1.30
D5	20.0 ± 0.5	19.64	13.5 ± 0.3	12.75	17.4 ± 0.4	12.39
D6	17.4 ± 0.5	14.19	11.7 ± 0.4	7.49	15.1 ± 0.5	7.14
D7	18.3 ± 0.5	16.13	12.4 ± 0.4	9.35	15.9 ± 0.5	8.99
D8	18.7 ± 0.6	14.63	12.6 ± 0.4	8.73	16.2 ± 0.5	8.42

Table 8. Calculated values of $\mu_{\mathrm{mass},\,i}$ for each detector and their compatibility indices r with the true values for Polyethylene (PE), PET, and ABS.

PE	D2	D3	D4	D5	D6	D7	D8
D2		13.88	12.32	17.38	14.96	15.83	15.61
D3	13.88		2.39	5.64	1.97	3.28	3.49
D4	12.32	2.39		7.95	4.27	5.58	5.62
D5	17.38	5.64	7.95		3.52	2.27	1.66
D6	14.96	1.97	4.27	3.52		1.25	1.61
D7	15.83	3.28	5.58	2.27	1.25		0.44
D8	15.61	3.49	5.62	1.66	1.61	0.44	

Table 9. Compatibilities of the attenuation coefficients for the polyethylene sample between different detectors. Compatibility values below or equal to 3 are shaded in `blue`; values above 3 are shaded in `red`, with proportional saturation.
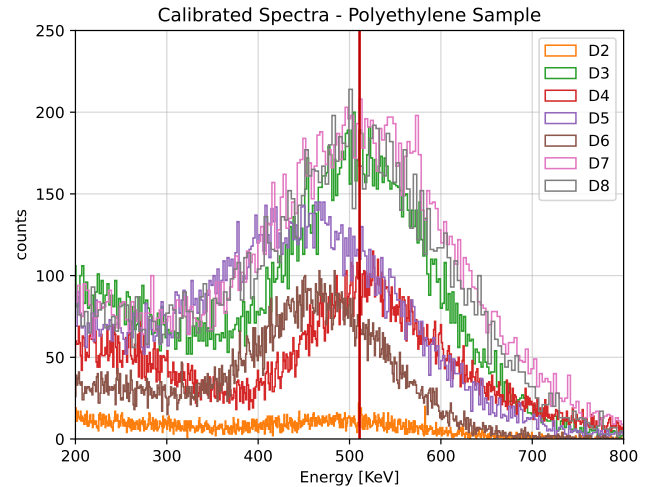
Figure 8. Calibrated spectra with the polyethylene sample. Also in this case, the D2 detector displays the lowest count rate.

As shown in Tab. 9, detector D2 remains highly incompatible with all other detectors, while D7, which is aligned with the source, exhibits good compatibility with D6 and D8. Excluding D2, the weighted average mass attenuation coefficient for polyethylene is $\langle\mu_{mass}^{\mathrm{PE}}\rangle = (13.0 \pm 0.2)$ mm^2/g. This value is highly incompatible with the expected value for polyethylene, with a compatibility index of $r_{\mathrm{PE}} = 28.32$. As we remarked before, the weighted average shows better compatibility with **ABS**, which has an expected mass attenuation coefficient $\overline{\mu}_{\mathrm{mass}}^{\mathrm{ABS}} = 11.3 \pm 0.1$ mm^2/g, which gives a compatibility index of $r_{\mathrm{ABS}} = 9.88$.

5.4 Graphite

The graphite sample used in the experiment had a measured thickness of $x_0 = (20.0 \pm 0.1)$ mm and a known density of $\varrho_{Gr} = 0.0017$ g/mm^3. The expected value of the mass attenuation coefficient for graphite is $\overline{\mu}_{\mathrm{gr}} = 8.715$ mm^2/g. Using these parameters, the mass attenuation coefficients $\mu_{\mathrm{mass},\,i}$ were calculated for each detector (D2 through D8), along with their compatibility with the theoretical value. The results are presented in Tab. 10, while the calibrated spectra for the graphite sample are shown in Fig. 9.

Detector	μ_{mass} [mm^2/g]	r
D2	45.6 ± 0.6	64.16
D3	8.5 ± 0.5	0.40
D4	6.9 ± 0.6	3.23
D5	5.5 ± 0.6	5.75
D6	6.6 ± 0.6	3.61
D7	6.9 ± 0.6	3.12
D8	6.0 ± 0.6	4.31

Table 10. Calculated values of $\mu_{\mathrm{mass},\,i}$ for each detector, along with their compatibility indices r. The best agreement with the expected value is observed for D3, with significant deviations noted for D2.
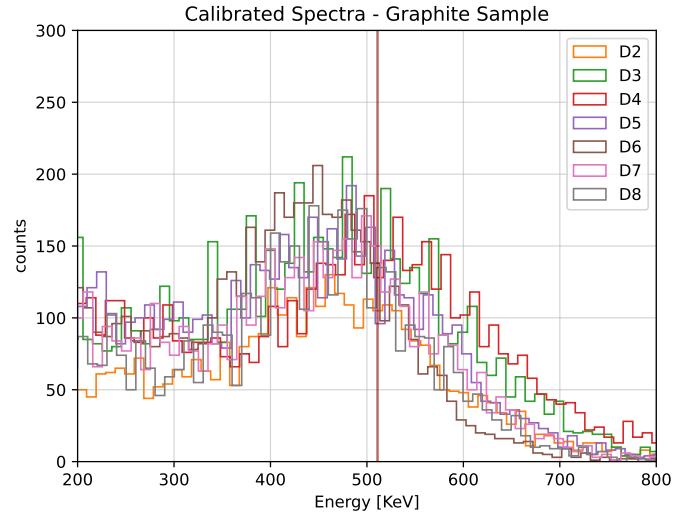
Figure 9. Calibrated spectra of the graphite sample, recorded using the updated experimental setup with a 15-minute acquisition.

Based on the updated acquisition data, the graphite sample shows a trend similar to that of the other materials. The mass attenuation coefficient calculated for detector D2 is clearly incompatible with the expected value, as shown in Tab. 10, and significantly deviates from the values obtained from the other detectors (see Tab. 11).

GR	D2	D3	D4	D5	D6	D7	D8
D2		48.98	47.99	50.22	47.21	46.72	46.74
D3	48.98		2.17	4.03	2.52	2.15	3.13
D4	47.99	2.17		1.71	0.39	0.04	1.01
D5	50.22	4.03	1.71		1.27	1.62	0.60
D6	47.21	2.52	0.39	1.27		0.34	0.62
D7	46.72	2.15	0.04	1.62	0.34		0.95
D8	46.74	3.13	1.01	0.60	0.62	0.95	

Table 11. Compatibilities of the attenuation coefficients for the Graphite sample between different detectors. Compatibility values below or equal to 3 are shaded in `blue`; values above 3 are shaded in `red`, with proportional saturation.

In this case, the best estimate is provided by detector D3. However, this result is not supported by the cross-compatibility analysis in Tab. 11, where the highest compatibility is once again observed near detector D7. This suggests that the result from D3 is likely an outlier and does not contradict the hypothesis of optimal alignment around D7.

The updated results represent a substantial improvement over the data from the initial acquisition run (presented in Appendix 8), but they still exhibit some discrepancies. These inconsistencies may be due to a slight misalignment of the sample or an error in the measured graphite thickness. Despite these issues, the weighted average of the mass attenuation coefficient for graphite is determined to be $\langle\mu_{\mathrm{mass}}^{\mathrm{GR}}\rangle = (6.8 \pm 0.2)$ mm^2/g, corresponding to a compatibility index of $r_{\mathrm{GR}} = 8.12$.
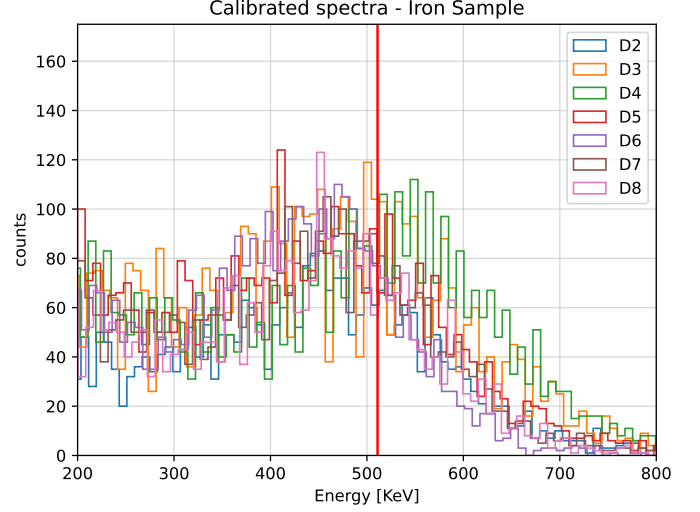
5.5 Iron

The iron sample used in the experiment had a measured thickness of $x_0 = (10.0 \pm 0.1)$ mm, and a known density of $\varrho_{\text{Fe}} = 0.00787$ g/mm^3. The expected mass attenuation coefficient for iron is $\overline{\mu}_{\text{Fe}} = 8.414$ mm^2/g. Using these parameters, the mass attenuation coefficients $\mu_{\text{mass}, i}$ were calculated for each detector (D2 through D8), together with their compatibility with the theoretical value. The results are presented in Tab. 12, while the calibrated spectra for the iron sample are shown in Fig. 10.

Detector	μ_{mass} [mm^2/g]	r
D2	33.4 ± 0.4	65.72
D3	9.2 ± 0.3	2.99
D4	8.3 ± 0.3	0.39
D5	7.2 ± 0.3	4.45
D6	8.4 ± 0.3	0.06
D7	9.1 ± 0.3	2.42
D8	8.4 ± 0.3	0.01

Table 12. Calculated values of $\mu_{\text{mass}, i}$ for each detector and their corresponding compatibility indices r. The compatibility coefficients indicate strong agreement for detectors D4, D6, and D8, while detector D5 exhibits significant incompatibility with the true value.

Figure 10. Calibrated spectra of the iron sample, recorded using the updated experimental setup with a 15-minute acquisition.

Fe	D2	D3	D4	D5	D6	D7	D8
D2		53.50	53.31	56.31	51.92	50.19	51.13
D3	53.50		2.27	5.30	1.87	0.04	1.88
D4	53.31	2.27		2.81	0.31	2.04	0.25
D5	56.31	5.30	2.81		3.04	4.77	2.92
D6	51.92	1.87	0.31	3.04		1.68	0.04
D7	50.19	0.04	2.04	4.77	1.68		1.69
D8	51.13	1.88	0.25	2.92	0.04	1.69	

Table 13. Compatibilities of the attenuation coefficients for the iron sample between different detectors. Lower values (shades of blue) indicate higher compatibility, while greater values (shades of red) indicate lower compatibility.

For the iron sample, the D2 detector is again completely incompatible with the true value, as shown in Table 12, and with the results of all other detectors, as shown in Table 13.

The alignment hypothesis between the source and the D7 detector is supported by the results for D6, D7, and D8, whose estimates of the mass attenuation coefficient are the most compatible with the true value and consistent with each other.

The weighted average mass attenuation coefficient for iron is $\langle \mu_{\text{mass}}^{\text{Fe}} \rangle = (8.4 \pm 0.1)$ mm^2/g, with a compatibility index of $r_{\text{Fe}} = 0.26$ relative to the true value.

6 Black box

In this part of the experiment, our objective was to investigate the attenuation properties of an unknown material concealed within a black box. Positioned between the ^{22}Na source and the detector column (D2 to D8), the black box was tested in five distinct and equidistant positions. For each configuration, we measured the count rates of the detectors, comparing the intensities observed with the black box to those from the reference measurement taken at the designated home position without the box, as already explained for the different samples in Sec. 4.1.

The resulting data were normalised to this reference, producing a 7×5 intensity matrix, where the rows correspond to the seven detectors and the columns represent the five positions of the black box. Each data acquisition of the five positions lasted 15 minutes. They were first calibrated; then the 511 KeV peak was fitted through a Gaussian curve and its integral within $\pm 2\sigma$ was taken as the value of N. The normalised intensity ratios I/I$_0$, where I and I$_0$ are calculated as explained in Eq. 2 are visualised as a heat map in Fig. 11 below, providing information on the spatial distribution of the attenuation caused by the material inside the black box.
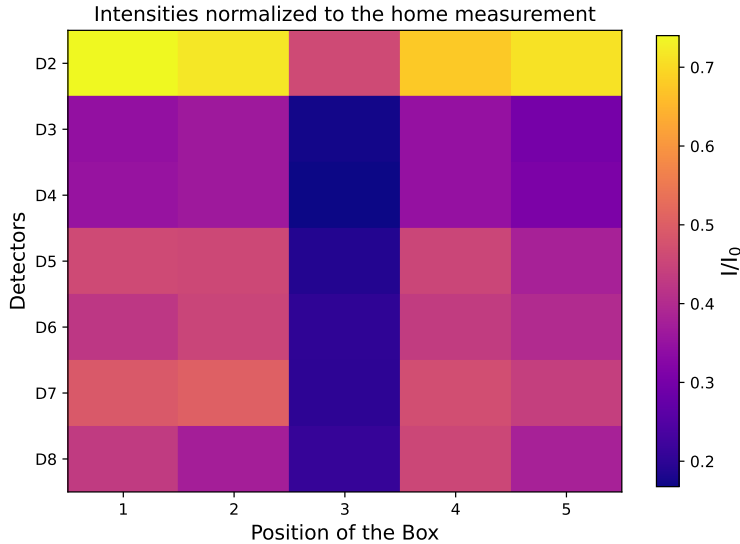
Figure 11. Heat map of the normalised intensities

Position number 3 exhibits a distinct behavior compared to the other positions, highlighting the presence of something inside the black box. Moreover, it is clear that, also in this part of the experiment, the D2 detector, being the farthest from the source, shows significant deviations compared to the other detectors. Nevertheless, it still follows the general trend, displaying a darker intensity in position 3, consistent with the behavior observed in the other detectors, but it will not be taken into consideration in the following analysis.

We can now compute the quantity $\mu \cdot x_{\text{eff}}$ as shown in Eq. 8 below; the results are shown in Tab. 14.

$$\mu \cdot x_{\text{eff}} = -\ln\left(\frac{I}{I_0}\right) \tag{8}$$

D3	D4	D5	D6	D7	D8
1.75 ± 0.02	1.79 ± 0.02	1.67 ± 0.02	1.59 ± 0.02	1.60 ± 0.02	1.55 ± 0.02

Table 14. $\mu \cdot x_{\text{eff}}$ values for detectors D3 to D8 in position 3

Subsequently, we divided $\mu_i \cdot x_{\text{eff},i}$ by the predetermined values of $\mu_{\text{mass}} \cdot \rho$ for lead, iron, aluminum, polyethylene, and graphite to calculate $x_{\text{eff},i}$ for each material and each detector. Finally, we divided $x_{\text{eff},i}$ by $\cos(\theta_i)$, following the inverse formula of Eq. 4, to obtain $x_{0,i}$, representing the expected thicknesses derived from the six different detectors from D3 to D8. The final estimate of x_0 was determined as the weighted average, considering the uncertainties[2].
The results are summarised in Tab. 15 below.

Material	Lead	Aluminum	Polyethylene	Graphite	Iron
x_0 [mm]	9.98 ± 0.08	78.9 ± 0.6	134 ± 1	141 ± 3	25.2 ± 0.2

Table 15. Expected thickness with different materials

Since the box has a maximum thickness of (22.0 ± 0.1) mm, aluminium, polyethylene, graphite and iron should be excluded. Hence we can guess that the hidden sample is a (9.98 ± 0.08) mm thick lead bar.

---

[2]Calculated analogously to Eq. 7.

7 Conclusions and possible further developments

The general analysis suggests a better alignment of the source with detector D7 showing greater consistency with theoretical expectations, while D2 exhibited significant anomalies due to its distance from the source. Additionally, an energy shift was observed in the acquired spectra compared to the calibration spectra, although it did not affect the further analysis; instead, the positioning of the samples relative to the collimator and detectors appears to have consistently influenced their data analysis.

This experiment successfully demonstrated the principles of digital imaging and the use of gamma-ray attenuation to identify materials and reconstruct their properties. Through the calibration of scintillation detectors, the mass attenuation coefficients of various materials were measured with reasonable accuracy, providing results that were largely consistent with theoretical expectations. The final results are shown in Tab. 16.

Material	Lead	Aluminium	Polyethylene	Graphite	Iron
$\langle \mu_{\text{mass}} \rangle$ [mm^2/g]	13.93 ± 0.08	7.9 ± 0.2	14.4 ± 0.2	21.1 ± 0.3	18.6 ± 0.2

Table 16. Final esteems for mass attenuation coefficients

The analysis revealed some systematic discrepancies, notably with detector D2, which exhibited significant deviations in count rates and attenuation measurements compared to other detectors. These anomalies were attributed to alignment issues and were excluded from the final weighted averages to ensure the reliability of the results.

The investigation of the black box effectively showcased the experimental setup's capability to differentiate materials based on their attenuation properties. The analysis concluded that the concealed sample was a lead bar with a thickness of (9.98 ± 0.08) mm, consistent with the physical constraints of the box and the theoretical attenuation coefficients.

An interesting avenue for future work involves leveraging machine learning techniques, such as neural networks, to enhance material identification. By constructing a comprehensive database containing attenuation data for a wide range of materials and thicknesses, a neural network could be trained to recognize both the material and its thickness based on the observed attenuation patterns. Such an approach could significantly improve the speed and accuracy of the analysis, making it a valuable tool for applications requiring rapid material characterization.

A practical starting point for building such a database is the NIST XCOM database[3], which provides theoretical mass attenuation coefficients for a variety of materials for different energy ranges. This data could be complemented with experimental measurements or simulations, such as those generated using Monte Carlo methods, to account for real effects like scattering, detector noise, and geometric misalignments. In particular these two following neural network architectures should be considered:

- **Multilayer Perceptron (MLP):** The input to the network could be a vector containing normalised attenuation values I/I_0 from multiple detectors, along with additional data such as photon energy and experimental geometry. The MLP would process these inputs through fully connected layers to output the predicted material type and thickness

- **Convolutional Neural Network (CNN):** The input would be an image-like representation of the data (for example a 2D matrix of attenuation values across detectors and positions, like the one shown in Fig. 11). Convolutional layers would extract spatial features, enabling the network to identify patterns indicative of specific materials and thicknesses.

The integration of such neural networks into the analysis could improve significantly material characterization, enabling real-time identification in complex scenarios, such as security screening or industrial quality control.

Overall, the experiment validated the theoretical framework of photon attenuation and demonstrated the practical application of coincidence detection and energy calibration in digital imaging. Future iterations could benefit from addressing the misalignment issues and exploring automated calibration techniques to enhance accuracy and reproducibility.

[3] https://physics.nist.gov/PhysRefData/Xcom/html/xcom1.html

8 Appendix

Below is the analysis of the first `incorrect` acquisition of graphite and iron. It is evident that the estimates are inaccurate, possibly due to the interference of other surrounding experiments, which may have disrupted the results, as already explained in Sec. 5.

8.1 First acquisition of graphite

It is reported below the calibrated spectra of graphite in Fig. 12, together with the mass attenutaion coefficients of each detector in Tab. 17.

Detector	μ_{mass} [mm^2/g]	r
D2	6.21 ± 0.6	4.03
D3	22.4 ± 0.4	35.44
D4	23.6 ± 0.4	36.80
D5	20.6 ± 0.4	32.24
D6	20.7 ± 0.4	31.09
D7	19.0 ± 0.4	28.00
D8	20.5 ± 0.4	27.28

Table 17. Calculated values of $\mu_{\mathrm{mass},\,i}$ for each detector and their corresponding compatibility indices r.
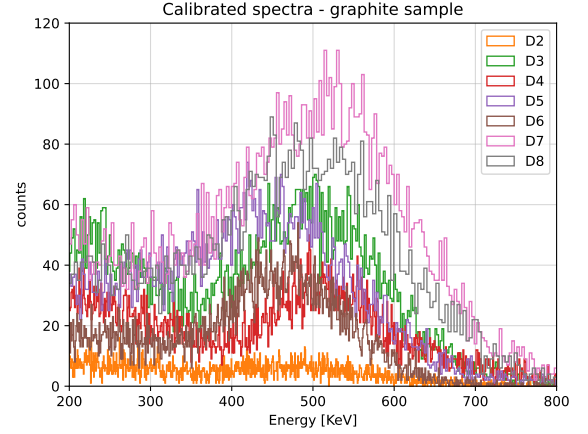
Figure 12. Calibrated spectra of the graphite sample, obtained with the old experimental setup. As stated above, the acquisition turned out to be incorrect.

Moreover one can examine the compatibility of the different esteems of the detectors presented in Tab. 18, which confirms that detector D2 is highly incompatible with all the others.

Gr	D2	D3	D4	D5	D6	D7	D8
D2		22.12	23.44	19.93	19.86	17.73	18.86
D3	22.12		2.14	3.33	6.34	3.33	3.33
D4	23.44	2.14		5.43	8.37	5.28	5.28
D5	19.93	3.33	5.43		3.07	0.26	0.26
D6	19.86	3.02	5.08	0.24		3.24	0.48
D7	17.73	6.34	8.37	3.07	3.24		2.57
D8	18.86	3.33	5.28	0.26	0.48	2.57	

Table 18. Compatibilities of the attenuation coefficients for the graphite sample between different detectors. Lower values (shades of blue) indicate higher compatibility, while higher values (shades of red) indicate lower compatibility.

8.2 First acquisition of iron

It is reported below the calibrated spectra of iron in Fig. 13, together with the mass attenutaion coefficients of each detector in Tab. 19.

Detector	μ_{mass} [mm^2/g]	r
D2	9.5 ± 0.3	3.55
D3	20.0 ± 0.2	59.44
D4	18.5 ± 0.2	53.48
D5	19.7 ± 0.2	58.90
D6	17.8 ± 0.2	50.14
D7	17.3 ± 0.2	49.56
D8	18.5 ± 0.2	47.04

Table 19. Calculated values of $\mu_{\text{mass},\,i}$ for each detector and their corresponding compatibility indices r.
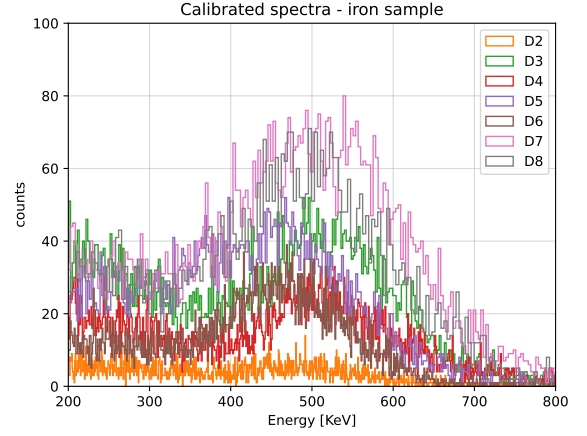
Figure 13. Calibrated spectra with the iron sample. As stated above, the acquisition turned out to be incorrect.

However, the strange behavior of D2 also appears in this case, as emerges in Fig. 13, where one can notice the low number of counts, and in Tab. 20 below, where D2 results are incompatible with all other detectors.

Fe	D2	D3	D4	D5	D6	D7	D8
D2		28.69	24.71	27.93	22.88	21.80	23.91
D3	28.69		5.73	1.24	8.25	10.17	5.14
D4	24.71	5.73		4.52	2.55	4.41	0.21
D5	27.93	1.24	4.52		7.06	8.99	4.00
D6	22.88	8.25	2.55	7.06		1.81	2.59
D7	21.80	10.17	4.41	8.99	1.81		4.31
D8	23.91	5.14	0.21	4.00	2.59	4.31	

Table 20. Compatibilities of the attenuation coefficients for the sample between different detectors. Lower values (shades of blue) indicate higher compatibility, while higher values (shades of red) indicate lower compatibility.